In-situ study of microstructures induced by the olivine to wadsleyite transformation at conditions of the 410 km depth discontinuity 🔓

Estelle Ledoux[1,*], Matthias Krug[2], Jeffrey Gay[1], Julien Chantel[1,§], Nadège Hilairet[1], Maxim Bykov[3,†], Elena Bykova[4,‡], Georgios Aprilis[5], Volodymyr Svitlyk[6,7], Gaston Garbarino[6], Nicolas Guignot[8], Carmen Sanchez-Valle[2], Sergio Speziale[9], and Sébastien Merkel[1]

[1]CNRS, INRAE, Centrale Lille, UMR 8207, UMET, Unité Matériaux et Transformations, Univ. Lille, F-59000 Lille, France
[2]Institute for Mineralogy, University of Münster, 48149 Münster, Germany
[3]Bayerisches Geoinstitut, University of Bayreuth, 95440 Bayreuth, Germany
[4]Deutsches Elektronen-Synchrotron DESY, Notkestr. 85, 22607 Hamburg, Germany
[5]Materials Physics and Technology at Extreme Conditions, Laboratory of Crystallography, Universität Bayreuth, D-95440 Bayreuth, Germany
[6]ESRF, The European Synchrotron Radiation Facility, 38000 Grenoble, France
[7]Helmhotz-Zentrum Dresden-Rossendorf, Institute of Resource Ecology, 01328 Dresden, Germany
[8]Synchrotron SOLEIL, L'Orme des Merisiers, Départementale 128, F-91190 Saint-Aubin, France
[9]GFZ German Research Centre for Geosciences, 14473 Potsdam, Germany

Abstract

The olivine-wadsleyite transformation is believed to occur at depths of about 410 km in the Earth, producing a major seismic discontinuity in this region of the Earth's mantle. The mechanism of this phase transition controls the microstructures of the newly nucleated wadsleyite, the major phase of the upper part of the mantle transition zone, and thus impacts seismic observations in the region. Here, we study the microstructures produced by the olivine-wadsleyite transformation using in situ laboratory experiments at pressures and temperatures relevant for the mantle transition zone. We transform pure olivine samples in laser-heated diamond-anvil cells at pressures ranging from 12.3 to 20.2 GPa and temperatures of 1400–1730 K. At different steps of the transformation we measure the orientation and size distribution of individual sample grains using multigrain crystallography at synchrotron radiation sources. We find that the olivine to wadsleyite transformation is incoherent at the conditions of the mantle transition zone, and is probably dominated by nucleation of wadsleyite at grain boundaries of the parent olivine. Thus, we expect that seismic anisotropy near 410 km would drop significantly due to the randomized lattice preferred orientation of newly nucleated wadsleyite induced by the incoherent transformation.

Keywords: Wadsleyite, phase transformation, multigrain crystallography, lattice preferred orientation, mantle transition zone, anisotropy

Introduction

The 410 km depth discontinuity in the Earth lies at the interface between the upper mantle and the mantle transition zone (MTZ) and plays a key role in regulating mantle flow and the distribution of water in the mantle (Bercovici and Karato 2003). It displays a sharp seismic velocity and density jump (Dziewoński and Anderson 1981), attributed to the pressure-induced phase transformation of olivine to wadsleyite (e.g., Ringwood 1991; Akaogi et al. 1989; Katsura and Ito 1989; Ito and Katsura 1989; Helffrich and Wood 1996; Katsura et al. 2004). The correlation between the depth of seismic reflections

and the pressure-temperature conditions of phase transitions in the $(Fe,Mg)_2SiO_4$ system (olivine-wadsleyite, wadsleyite-ringwoodite, and ringwoodite-bridgmanite) has been used to estimate the temperatures at mantle discontinuities and anchor deep Earth thermal profiles (e.g., Katsura et al. 2004, 2009).

Phase transitions will also affect the microstructure of a rock and large-scale geophysical observations. Incoherent transformations, i.e., transformations following no orientation relationship between the parent phase and the daughter phase, will erase the microstructures of the parent rock, while coherent transformations, i.e., transformations where the daughter phase grows with an orientation related to the parent phase, will preserve some microstructures in the daughter rock, inherited from the parent rock. In the case of the olivine-wadsleyite transition, both mechanisms have been reported (e.g., Smyth et al. 2012).

Phase transformations in olivine will affect observations of seismic signals from the deep mantle, such as anisotropy or reflections off the interface, in regions where the material is downwelling. A coherent olivine-wadsleyite transition will

preserve lattice preferred orientation (LPO) in the newly formed wadsleyite-rich rock below the discontinuity. In contrast, the incoherent transformation of olivine into wadsleyite will erase LPO and hence anisotropy of the parent olivine-rich rock [as reported in Yuan and Beghein (2013), for instance]. The effect of microstructures on the underside reflections at the 410 km depth discontinuity was investigated by Saki et al. (2018), and it was shown that LPO in olivine above the discontinuity would in fact affect seismic observables. Microstructures in wadsleyite below the discontinuity, however, will be affected by the nature of the olivine-wadsleyite phase transition and deformation of wadsleyite itself. Thus, the nature of the olivine-wadsleyite transformation will play an important role in the physical properties of the Earth's mantle and their monitoring by geophysical observables.

In addition, a phase transformation affects grain sizes (e.g., Rosa et al. 2016; Perrillat et al. 2013), which will also affect the properties and behavior of the rocks. Rozel (2012), for instance, showed that a grain size-dependent rheology dramatically affects the convection regime of telluric planets. Mohiuddin et al. (2020) also showed that the direct olivine to ringwoodite transformation at low temperatures induces a fine-grained ringwoodite aggregate, deforming by diffusion creep, and with a substantial strength reduction and a weakening of cold subducted slabs. As such, grain size evolution during phase transitions in the olivine system is important to model the mechanical behavior of the mantle and the dynamics of subduction in the MTZ.

Studies of phase transformation microstructures in olivine were first performed on analogs, mostly germanates, due to experimental limitations (e.g., Ringwood 1958, 1962; Vaughan and Coe 1981; Ross and Navrotsky 1987; Burnley and Green 1989; Ringwood and Seabrook 1962). In germanate analogs, however, the α ("olivine") phase directly transforms to the γ ("ringwoodite") polymorph, with no intermediate β ("wadsleyite") phase. Hence, the olivine-wadsleyite transformation microstructures require studies on the $(Fe,Mg)_2SiO_4$ system itself.

Experiments on the olivine-wadsleyite transformation generally indicate an incoherent nucleation and growth mechanism, where no relation between parent olivine and newly formed wadsleyite is observed (Brearley et al. 1992; Kerschhofer et al. 1996, 1998; Kubo et al. 1998b, 2004; Smyth et al. 2012; Mohiuddin and Karato 2018). In addition, Kerschhofer et al. (1998) have shown that incoherent nucleation of wadsleyite is dominant at olivine grain boundaries in small grain (<10–20 μm) aggregates, while in large crystals (0.6 mm) intracrystalline incoherent nucleation is dominant. Mohiuddin and Karato (2018) also observed both of these mechanisms in San Carlos olivine polycrystals of ~25 μm grain size and proposed that the dominance of one mechanism over the other also depends on the temperature and the overpressure in the sample. These two incoherent mechanisms lead to slightly different microstructures. Grain boundary nucleation is expected to produce grains with random shapes while intracrystalline nucleation produces lamellae-shaped wadsleyite grains (Kerschhofer et al. 1996, 1998; Mohiuddin and Karato 2018) along olivine stacking faults on planes (010) (Kerschhofer et al. 1996) or {101} (Kerschhofer et al. 1998), possibly resulting in shape preferred orientation of wadsleyite grains.

Finally, the study of Smyth et al. (2012) documented both coherent and incoherent deformation mechanisms. By heating and compressing a fine-grained mixture of natural olivine, silica, FeO, and brucite $[Mg(OH)_2]$ at 13 GPa and 1400 °C in a multi-anvil press, they synthesized an aggregate composed of olivine, wadsleyite, clinoenstatite, and a melt phase. Quenched samples were then recovered for ex-situ analysis. Transmission electron microscopy studies of these samples show that small lamellae of wadsleyite were present within the remaining olivine crystals with the two following crystallographic relations to the host: Type I with $[001]_{ol} \parallel [010]_{wd}$ and $(100)_{ol} \parallel \{101\}_{wd}$, and Type II with $[001]_{ol} \parallel [100]_{wd}$ and $(100)_{ol} \parallel \{021\}_{wd}$. Nevertheless, the authors observed a dominance of incoherent grains of wadsleyite. They hence concluded that the coherent mechanisms, although active, are less efficient than the incoherent nucleation of wadsleyite and should, hence, not have a significant impact on the microstructure.

Previous studies on the mechanisms of olivine-wadsleyite transformation, however, mostly relied on post-mortem characterization at the local scale using optical or electron microscopy (Brearley et al. 1992; Kerschhofer et al. 1996, 1998; Kubo et al. 1998a, 1998b, 2004; Smyth et al. 2012; Mohiuddin and Karato 2018). Ex-situ techniques allow a very precise determination of crystallographic orientations, compositions, grain boundaries, mean grain sizes, and defect structures but questions remain on whether the sample microstructures are modified at the later stages of the experiment, during decompression for instance, and whether orientation relationship at the local scale does affect microstructures at the bulk scale, in a polycrystal. Only a few in situ results of transformation-induced microstructures were reported (Wenk et al. 2004; Rosa et al. 2016; Chandler et al. 2021b), but all were performed at fairly low temperatures and focus on the olivine-ringwoodite direct transformation, rather than the olivine-wadsleyite transformation, which requires higher temperatures.

In this work, we re-address the question of microstructures induced by the olivine-wadsleyite transformation using in situ measurements at high pressure and temperatures. We rely on a recently developed DAC-based experimental method, multigrain crystallography (MGC) (Nisr et al. 2012, 2014; Zhang et al. 2019; Langrand et al. 2017), which allows in situ measurements of crystallographic structures, grain orientations and grain statistics at high pressure during processes, such as deformation or phase transformation. Previous works using MGC did not succeed to maintain relevant mantle temperatures (Rosa et al. 2015; Langrand et al. 2017; Zhang et al. 2019; Chandler et al. 2021a, 2021b). Here, olivine both as single-crystal and polycrystal is compressed at temperatures close to those of a standard geotherm using a laser-heated DAC, and transformed into the wadsleyite phase. We follow the microstructures prior to, during, and after the transformation using MGC and, based on these microstructures, we determine which type of transformation occurs in olivine at the pressures and temperatures of the MTZ.

METHODS

Samples

Two starting materials were used: an olivine single crystal and sintered polycrystalline olivine samples. The olivine single-crystal was a fragment of natural San Carlos olivine, with dimensions of ~20 × 20 μm and polished manually to obtain a thickness of 10–15 μm. The polycrystalline samples were prepared from a powder of

natural San Carlos olivine, ground in a planetary mill and sintered at 500–600 MPa and 1500 K for 40 min in a piston-cylinder apparatus. A piece of the sintered product was then prepared for electron microscopy and characterized in a FEG JEOL JSM-7800F scanning electron microscope (SEM) using the electron backscattered diffraction (EBSD) technique. This characterization shows that it is a pure olivine polycrystal with heterogeneous grain sizes, ranging between less than a micrometer and 50 μm, and with no preferred orientation (Figs. 1a and 1b). Infrared analysis shows <3 ppm of H_2O in the olivine grains of the sintered polycrystal (Fig. 1c). That analysis was done with a Bruker Hyperion 3000 FTIR microscope coupled with a Vertex 70 spectrometer, which was equipped with a simple MCT detector and a "focal plan array" detector. Once sintered, the product was cut into fine slices with a precision diamond wire saw and mechanically polished to a thickness of 10–15 μm. Finally, samples were cut into disks of 20 μm diameter by lasers (Fig. 1d).

In both cases, samples were coated with a 150–200 nm thick platinum layer on both sides. This step ensures proper absorption of the heating infrared lasers by the sample. It is also critical to maintain stable temperatures as olivine and wadsleyite have different optical absorption properties. No signal from the platinum coating is seen in the diffraction images because of the very small volume fraction of platinum compared to the sample. Nevertheless, temperature stability during laser heating was drastically improved for samples with platinum coating. Earlier attempts with un-coated samples showed jumps in temperatures of several hundreds of degrees during pressure increases or phase transformations and those data sets were systematically discarded. Such large temperature oscillations did not occur when using samples coated with platinum. The platinum coating is then a convenient way of increasing the stability of the heating without decreasing the diffraction signal of the sample.

High-temperature/high-pressure experiments

To reach the high pressure and high temperature of the 410 km depth discontinuity, we use diamond-anvil cells (DAC) coupled with laser heating (Fig. 2). We used diamonds with 300 μm flat tips, rhenium gaskets with holes of 100–145 μm in diameter to serve as sample chambers (Fig. 1d), and membranes to control sample pressure remotely. As pressure media, we used either MgO, KCl, or alumina (Table 1). All three are chemically inert in an olivine-wadsleyite system at the investigated pressure-temperature conditions (Shen and Lazor 1995; Kimura et al. 2017; Zhou et al. 2020). We can rule out undesired reactions in our experiments as no other phase than olivine, wadsleyite and the pressure media are present in the diffraction patterns (Fig. 3). In all cases, the sample and pressure media were loaded under a controlled argon atmosphere into the DAC to prevent the interaction of the hygroscopic pressure transmitting media with air moisture.

The state of the sample was followed using in situ multigrain X-ray diffraction at the ID27 beamline at ESRF, the P02.2 beamline at PETRA III, and the PSICHÉ beamline at SOLEIL. In all cases, olivine was compressed at ambient temperature up to pressures between 2 and 10 GPa, after which we laser-heated to achieve temperatures ranging between 1400 and 1800 K. Pressure was then slowly increased while maintaining a constant temperature within ±100 K. The sample composition and pressure were monitored from the 2D-diffraction patterns using the software Dioptas (Prescher and Prakapenka 2015). Sample temperatures were measured using spectral radiometry as provided by the beamlines during the experiments. At several points upon compression, pressure increase was stopped to collect multigrain X-ray diffraction data by rotating the DAC over Δω ≈ 60° (depending
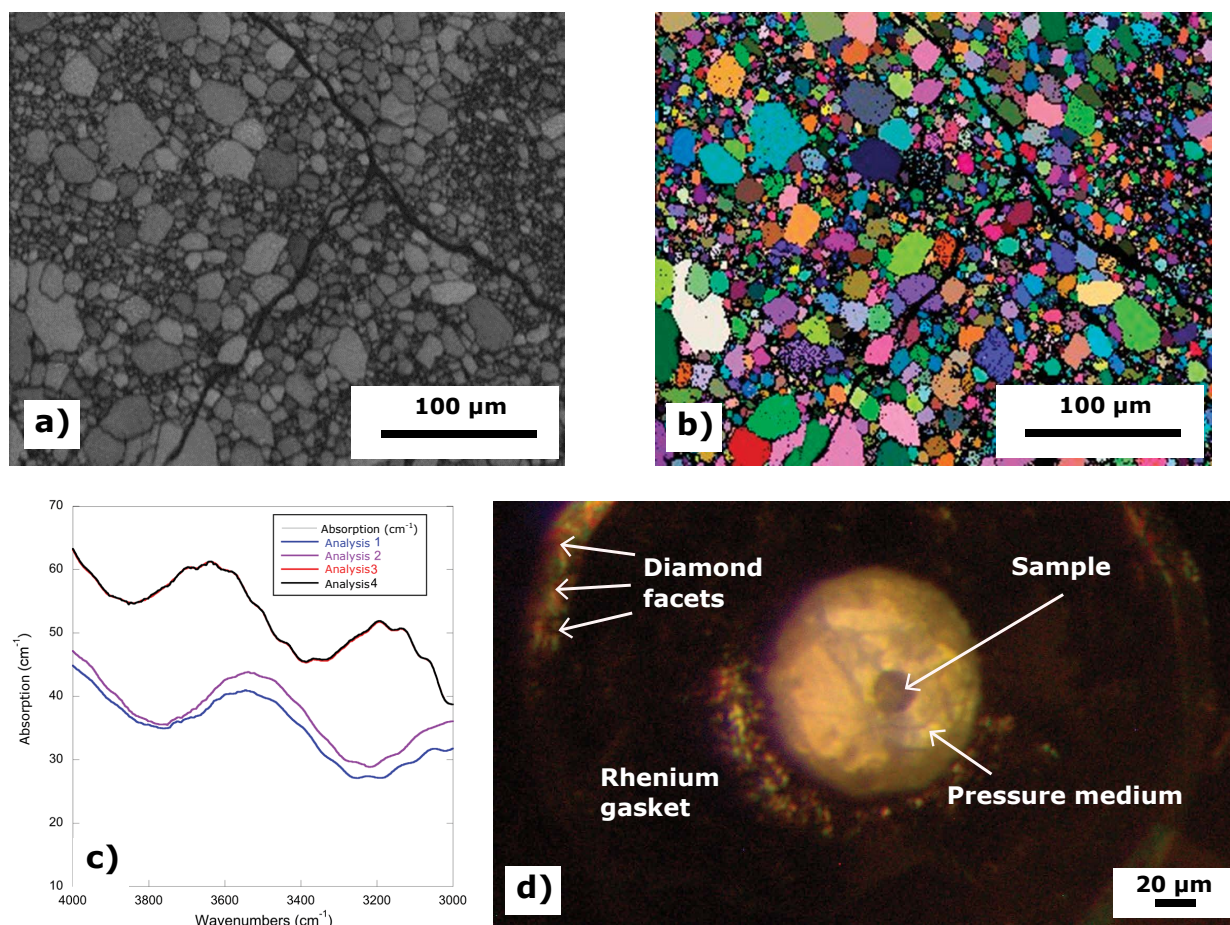
FIGURE 1. Characterization of the polycrystalline starting material for experiments at ESRF and PETRA III. (**a**) EBSD band contrast image showing the shapes and sizes of the grains in the olivine polycrystal after piston-cylinder sintering. (**b**) EBSD orientation map of the starting material. (**c**) FTIR measurements of water content in grains of the sintered polycrystal. (**d**) Photograph of the diamond-anvil cell pressure chamber (closed cell, top view). The olivine polycrystalline sample is a 20 μm diameter disk loaded with a MgO pressure medium inside a 140 μm diameter hole in a rhenium gasket.

TABLE 1. List of samples and experiments

| Experiment	Starting material	PTM	Beamline	Characterization technique
Olivine_01	Single crystal	Alumina	SOLEIL-PSICHÉ	MGC after temperature quench
LTC_05_01	Polycrystal	MgO	ESRF-ID27	In situ MGC at high temperature
LTC_03_02	Polycrystal	MgO	ESRF-ID27	In situ MGC at high temperature
P2_01	Polycrystal	KCl	PETRA-III-P02.2	In situ MGC at high temperature

Note: PTM = pressure transmitting medium.

on diamond height and cell opening) and acquiring X-ray diffraction images every 0.5° rotation increment δω (Fig. 2). At both ESRF-ID27 and PETRA-III-P02.2, laser heating was maintained during multigrain X-ray diffraction data collection, using the standard laser-heating configuration at ESRF, and using a device such as that presented in Bykova et al. (2019) at PETRA-III. At SOLEIL-PSICHÉ the sample was quenched to ambient temperature before multigrain X-ray diffraction data collection. Sample recrystallization could occur during the high-temperature 3D-XRD scans. Note, however, that recrystallization is most expected in deformed grains with high concentrations of internal defects (e.g., Poirier and Guillopé 1979; Urai et al. 1986), and hence parent olivine rather than the newly nucleated wadsleyite grains. In situ 3DXRD measurements at high temperature, nevertheless, offer the great advantage to avoid introducing additional deviatoric stresses upon temperature quenching that could, also, affect the sample (Kavner and Duffy 2001).

At the P02.2 beamline at PETRA III, X-rays were set to a wavelength of 0.2903 Å and focused to 7.6 (horizontal) × 4.4 (vertical) μm. The sample-to-detector distance was 398.7 mm, based on the CeO_2 calibration. Diffraction images were collected using a PerkinElmer XRD 1621 amorphous silicon flat-panel detector with 2048 × 2048 pixels of 200 × 200 μm (Liermann et al. 2015) for 5 s. At the ID27 beamline at ESRF, we used X-rays with a wavelength of 0.3738 Å, focused to 3.2 (horizontal) × 3.0 (vertical) μm. The sample-to-detector distance was 245.54 mm, based on the CeO_2 calibration. Diffraction images were collected using a MAR165 CCD planar detector with 2048 × 2048 pixels of 79 × 79 μm for 6 s. At the PSICHÉ beamline at SOLEIL, we used X-rays with a wavelength of 0.3738 Å focused to about 12 (horizontal) × 10 (vertical) μm. The sample-to-detector distance was 389.75 mm, based on the CeO_2 calibration. Diffraction images were collected employing a PILATUS flat-panel detector with 1475 × 1679 pixels of 172 × 172 μm, and with an acquisition time of 5 s. Note that the diffraction study of large single crystals was allowed by the PILATUS detector that can count every photon received on the panel, with high peaks spread resolution and a small readout time (Eikenberry et al. 2003), and can handle significantly higher peak intensity before saturation.

Table 1 summarizes the experiments that were performed along with the starting materials, pressure-transmitting media, and sample characterization techniques. Three experiments used pure polycrystalline olivine samples as starting materials: LTC_05_01 and LTC_03_02 performed on ESRF-ID27 and P2_01 performed on PETRA-III-P02.2. One experiment started from an olivine single-crystal, Olivine_01 performed at SOLEIL-PSICHÉ.
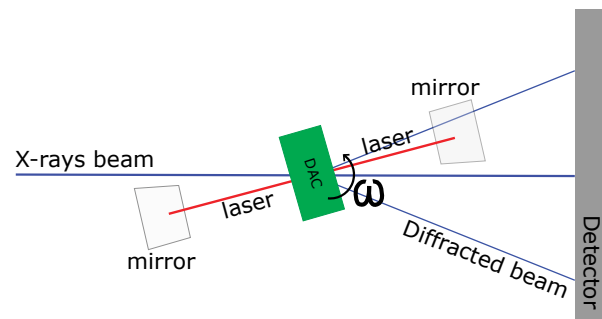

FIGURE 2. Experimental layout for multigrain crystallography (MGC) measurements at high pressure and high temperature at a synchrotron beamline. View from the top. The synchrotron X-rays beam (thick blue line) passes through the DAC (in green) and is transmitted or diffracted by the crystallites in the sample. The diffracted rays (thin blue lines) form the diffraction pattern on the detector (in gray). The DAC is rotated in ω and data are collected at different ω values. In the reported experiments at both PETRA-III-P02.2 and ESRF-ID27, the laser heating system was rotating with the DAC during ω rotations. At SOLEIL-PSICHÉ, the lasers were fixed and the sample was quenched in temperature before collecting MGC data.

Diffraction data processing

Post-experiment, ω-rotation multigrain diffraction images were stacked to generate an average diffraction image, which was then further processed using the Rietveld refinement package MAUD (Lutterotti et al. 2014; Wenk et al. 2014) from which we extract the unit-cell parameters of the pressure medium, olivine, and wadsleyite. The pressure was then calculated using thermal equations of state from the literature [Angel et al. (2018) for olivine and Katsura et al. (2009) for wadsleyite] and the EosFit Calculator software (Angel et al. 2014). Pressure and temperature conditions for each multigrain measurement are summarized in Table 2.

The sample microstructural evolution during the transformation is processed using multigrain crystallography (MGC). This method involves acquiring 2D-diffraction images at different ω rotation angles. The data are then processed to:
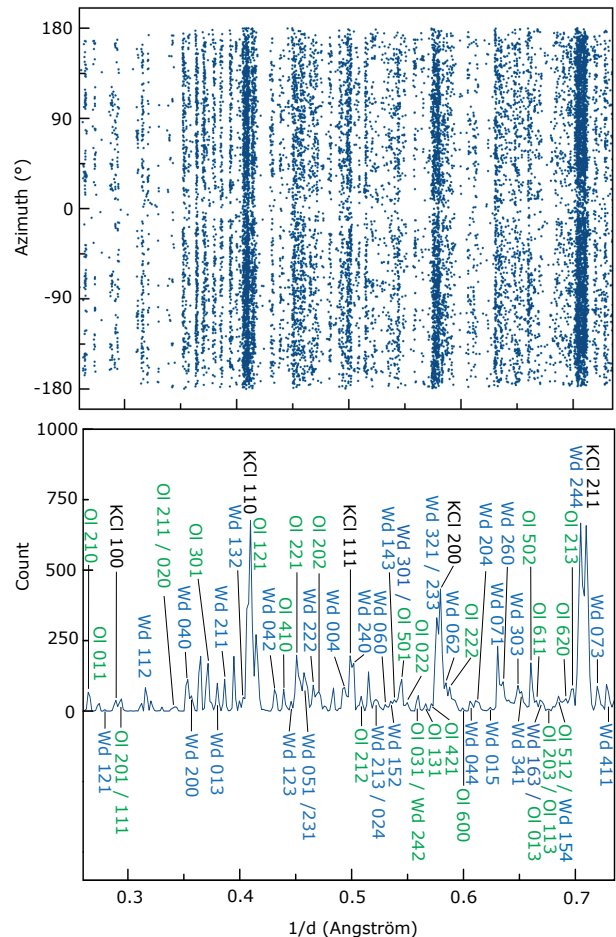
FIGURE 3. Experimental diffraction data for data set P2_01_s07 where olivine and wadsleyite coexist. (**a**) Diffraction spots extracted by the 3D-XRD process from the whole diffraction collection, plotted in azimuth vs. inverse *d*-spacing and staked in omega. (**b**) Integrated diffraction pattern with annotated diffraction peaks for KCl, olivine, and wadsleyite. Here, the diffraction pattern is plotted as a histogram of locations of the diffraction spots shown in (**a**) vs. inverse of the *d*-spacing. Using such a histogram leads to sharp diffraction signals and allows for easy sample identification.

TABLE 2. Experimental conditions and indexing statistics

Experiment	Collection	P (GPa)	T (K)	Phase	N	Mean GR (µm)	GVE per grain	Indexed GVE
Olivine_01	multi1	6.3	300	Olivine	1	6.1	75.0	19.9%
	multi4	16.1	300	Olivine	25	0.8(3)	31.0	16.4%
				Wadsleyite	72	0.8(3)	31.7	42.6%
LTC_05_01	s26	14.9	1400	Olivine	55	0.5(3)	37.9	23.3%
	s27	18.7	1730	Wadsleyite	114	0.6(3)	39.0	46.4%
LTC_03_02	s07	17.0	1700	Olivine	180	0.5(3)	46.9	58.7%
	s08	18.8	1700	Wadsleyite	188	0.5(3)	49.4	63.2%
P2_01	s06	20.2	1550	Olivine	84	1.0(4)	122.4	47.6%
	s07	13.5	1510	Olivine	83	0.7(3)	119.1	46.8%
				Wadsleyite	30	0.7(2)	123.7	17.0%
	s08	12.3	1450	Wadsleyite	144	0.7(3)	47.4	76.2%

Notes: For each experiment, the table indicates the pressure (*P*)/temperature (*T*) conditions at which multigrain measurements were performed, together with the results of the multigrain crystallography indexing: number of indexed olivine or wadsleyite grains (N), the mean radius of the indexed grains (mean GR), the mean number of indexed reflections per grain (GVE per grains), and percentage of indexed G vectors for each phase (Indexed GVE). Note that other phases, such as the pressure medium, might also be the source of a large number of G vectors that overlap with those of the phase of interest and will reduce the apparent percentage of indexed G vectors. Also note that the mean grain radius deduced from MGC in experiment Olivine_01 is limited by the size of the incoming X-ray beam, and hence smaller than that of the original single-crystal. Numbers in parenthesis are standard deviations from the mean grain size, on the last digit.

(1) separate the background and the diffraction signals of the pressure medium from that of the larger sample grains; (2) identify individual diffraction spots of the larger sample grains; and (3) determine the sample grain orientation matrices. The detailed procedure has been described in Rosa et al. (2015) and used in Rosa et al. (2016) and Langrand et al. (2017). It relies on open-source softwares from the FABLE-3DXRD package, available online at https://github.com/FABLE-3DXRD, additional tools from the TIMEleSS project, available online at https://github.com/FABLE-3DXRD/TIMEleSS, and thoroughly described in a dedicated manual at http://multigrain.texture.rocks/.

Individual diffraction images are first cleaned to exclude high-intensity single-crystal diffraction spots from the diamond anvils and subtract the background signal. Individual diffraction spots are then located using a high-pass filter, as implemented in the Peaksearch algorithm (Sörensen et al. 2012). The ImageD11 software (Wright 2006) then uses the list of extracted diffraction spots and information on the experimental conditions to compute a list of potential G-vectors to be assigned to the sample grains. ImageD11 does not include full crystallographic information to generate the list of G-vectors and hence generate Miller indices which can be extinct in a given crystal structure. We hence re-evaluate the list of potential G-vectors using our TIMEleSS scripts and the full crystallographic information for olivine and wadsleyite, and concentrate on G-vectors that will actually contribute to diffraction. This additional step decreases the risk of error during grain indexing. At this point, each observed G-vector is assigned to its observed intensity and location in orientation space (2θ, η, and ω angles), and potential *h*, *k*, and *l* Miller indices.

The final indexing step relies on the GrainSpotter software (Schmidt 2014), with the following settings: 100 000 random grain orientation trials, tolerances of 0.08° in 2θ, 4° in η and 3° in ω to assign a measured G-vector to a grain, a minimum number of 15 G-vectors per grain, and a minimum completeness of 30%. This procedure is repeated several times (i.e., 50), removing already assigned G-vectors, to improve the number of indexed grains. The final output consists of a list of grains, along with their crystallographic orientation and the list of the associated diffraction spots.

From the results of the MGC processing, it is possible to extract a relative size for the indexed grains by scaling grain volume to the intensity of their diffraction spots. Then, using the illuminated volume of the sample, the number of indexed grains and their relative volumes, we can provide an estimate of their actual size, as volume or mean radius. This computation is performed using a script from the TIMEleSS tools.

The raw multigrain data, as well as the resulting lists of grains, their orientation and grain size are available online at https://doi.org/10.57745/NZFWP9 (Ledoux et al. 2023).

Grain orientations analysis

Indexed grain orientations are shown as either pole figures (PF) (for samples with very few grains, e.g., Fig. 4) or inverse pole figures (IPF) of the compression direction (for samples with a large number of grains, e.g., Fig. 5). Each marker in inverse pole figures represents an indexed orientation and is color-coded according to calculations based on an orientation distribution function (ODF) fitted to the indexing results. Markers in pole figures also represent the orientation of indexed grains but are not color-coded because orientation distributions are not relevant for a low number of grains. For this step, we use the open-source MTEX toolbox for MATLAB (Bachmann et al. 2010).

MTEX is also used to test the effect of a coherent transformation mechanism from olivine to wadsleyite. For these simulations, we start from the indexed olivine grain orientations prior to the transformation and compute the daughter wadsleyite orientations resulting from a strict coherent transformation. We test for both orientation relationships suggested by Smyth et al. (2012): Type I with $[001]_{ol} \parallel [010]_{wd}$ and $(100)_{ol} \parallel \{101\}_{wd}$, and Type II with $[001]_{ol} \parallel [100]_{wd}$ and $(100)_{ol} \parallel \{021\}_{wd}$. The simulated daughter wadsleyite orientations are also plotted as IPF, using the same procedure described above.
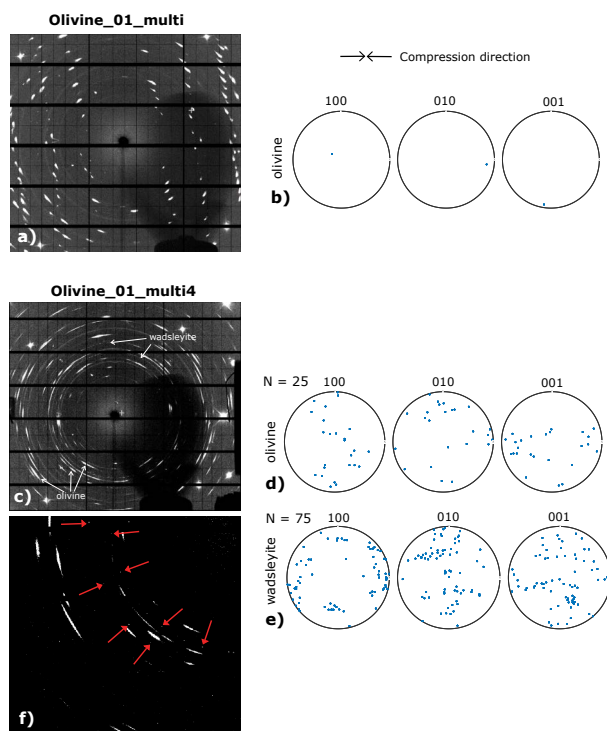
FIGURE 4. Transformation microstructures starting from an olivine single crystal. Single-crystal olivine data (**a** and **b**), olivine-wadsleyite polycrystal data after partial transformation (**c**, **d**, and **e**). Stacked diffraction patterns (**a** and **c**). (100), (010), and (001) pole figures representing the orientations of olivine (**b** and **d**) and wadsleyite grains (**e**). The compression direction is indicated above the pole figures. To better illustrate the diffraction spots of the wadsleyite grains, a zoom-in for one image at one omega step of the collection is shown (**f**).

FIGURE 5. Transformation microstructures in polycrystalline olivine samples. Inverse pole figures of the compression direction representing grain orientations of olivine (Ol) before transformation, olivine (Ol) and wadsleyite (Wd) during transformation, and wadsleyite (Wd) after transformation from olivine. LTC_05_01, LTC_03_02, and P2_01 are different experiments. Pressure and temperature conditions of the measurements are indicated below each inverse pole figure along with N, the number of indexed grains. The fundamental space and axes defining the inverse pole figure are shown on the right. The color scale applied to the markers is based on a probability calculated from the orientation distribution function fitted to the sample and is expressed in multiple of a random distribution (m.r.d.). It should be noted that, in all the experiments in this figure, MGC data collections were performed in situ at high *P-T* conditions during laser-heating.
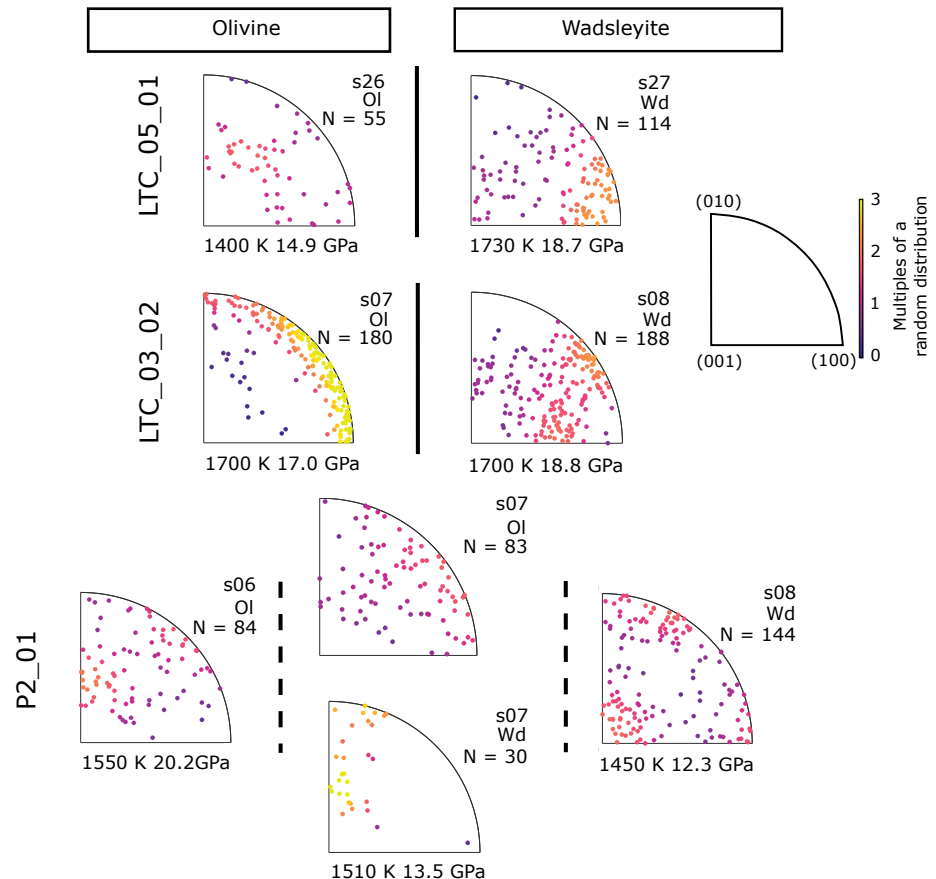
RESULTS

Transformation microstructures in olivine single crystal

Sample in run Olivine_01 was an olivine single crystal at 6.3 GPa and 300 K. It was laser-heated to temperatures of 1700–1800 K and compressed at 1700–1800 K over 100 min to drive a partial conversion to wadsleyite. Multigrain crystallography data was collected on the olivine single-crystal prior to the pressure increase, and at 16.1 GPa and 300 K, after the partial transformation to wadsleyite and quench in temperature (Fig. 4).

Before the transformation (Figs. 4a and 4b), the sample is an olivine single crystal, as shown by both the diffraction pattern and the single-grain orientation deduced from the multigrain crystallography processing. The diffraction image shows intense and slightly deformed diffraction peaks, indicating that the crystal is large and is submitted to some stress. The multigrain crystallography processing locates a single grain, with an estimated equivalent radius (i.e., the radius of a sphere with an identical volume to that of the grain) of 6.1 μm.

Later, upon compression at high temperature (Figs. 4c–4f) the sample contains both olivine and wadsleyite. Olivine diffraction peaks are still intense (Fig. 4), indicating grains of larger size, but also appear elongated along the diffraction rings, suggesting that the olivine portion of the sample is subdividing into different orientation domains. The multigrain crystallography processing identifies 25 grains of olivine with a mean radius of 0.8 μm. The orientations of these grains do not show any particular alignment with specific sample directions, but are different from the orientation of the original single crystal, before partial transformation to wadsleyite (Fig. 4b). On the stack of all ω diffraction patterns, wadsleyite appears as small diffraction peaks forming a nearly continuous diffraction ring, suggesting that wadsleyite grains are small. On a single image of the collection, however, the diffraction spots of wadsleyite are distinct (Fig. 4f). The multigrain crystallography processing locates 72 daughter orientations of wadsleyite, with a mean radius of 0.8 μm. Most of these grains show a cluster of orientation with their [100] crystallographic axes in the vicinity of the compression direction (Fig. 4e).

Transformation microstructures in polycrystalline olivine

Samples in runs LTC_05_01, LTC_03_02, and P2_01 were pure polycrystalline olivine. All were compressed at temperatures ranging between 1400 and 1730 K and converted to wadsleyite. Figure 5 presents the orientations of the grains indexed by MGC in these three experiments and at different steps of the transformation.

In experiment LTC_05_01, the transformation from olivine to wadsleyite is observed between 1400 K–14.9 GPa and 1730 K–18.7 GPa. Before transformation (collection s26), MGC indexes 55 olivine grains with a mean grain radius of 0.5 μm and no lattice preferred orientation. After the transformation (collection s27), MGC locates 114 grains of wadsleyite with a mean grains radius of 0.6 μm. We observe significant crystal preferred orientations, with the [100] crystallographic axes of

wadsleyite aligned at a low angle of the compression direction.

In experiment LTC_03_02, the transformation from olivine to wadsleyite is observed at 1700 K and between 17.0 and 18.8 GPa. Before the transformation (collection s07), MGC indexes 180 grains of olivine with a mean grain radius of 0.5 μm. The olivine grain orientations form a girdle between the (100) and (010) poles of the inverse pole figure. After the transformation (collection s08), 188 grains of wadsleyite are indexed with a mean grain radius of 0.5 μm and a crystal preferred orientation with the maximum orientation probability 30° away from (100).

In experiment P2_01, the transformation from olivine to wadsleyite is observed between 1550 K–20.2 GPa and 1450 K–12.3 GPa. Before the transformation (collection s06), MGC indexes 84 olivine grains with a mean grain radius of 1.0 μm and no crystal preferred orientations. In this experiment, pressure decreased at the olivine to wadsleyite conversion, with data collected while olivine and wadsleyite coexist (collection s07) leading to 83 olivine grains with a mean grain radius of 0.7 μm and no crystal preferred orientation and 30 wadsleyite grains with a mean grain radius of 0.7 μm and orientations concentrated between the (010) and (001) poles of the inverse pole figure. After full conversion to wadsleyite (collection s08), we index 144 wadsleyite grains with a mean grain radius of 0.7 μm. The crystal preferred orientation is weak but shows several maxima at (001), (010), and (001) in the inverse pole figure.

Grain size evolution

Two tendencies are observed regarding grain size evolution in our experiments: (1) in experiments Olivine_01 and P2_01, the mean sample grain size decreases during the phase transition from olivine to wadsleyite, while (2) in experiments LTC_03_02 and LTC_05_01, the grain size does not significantly change during the phase transition.

The grains size evolution in experiments Olivine_01 and P2_01 is illustrated in Figure 6, based on the example of experiment P2_01 for which data with coexisting olivine and wadsleyite is available. Before the transformation (data set s06), the olivine grain radii vary between 0.5 and 2.2 μm. During the transformation, the olivine grain size decreases, with grain radii between 0.4 and 1.6 μm (data set s07). Coexisting wadsleyite in the same measurement shows grain radii between 0.4 and 1.1 μm. After the transformation (data set s08), the sample is made of wadsleyite grains with grain radii ranging between 0.2 and 1.8 μm and an average radius of 0.7 μm.

Regarding experiments LTC_03_02 and LTC_05_01, for which grain size does not reduce upon the phase transformation to wadsleyite, we can notice that the average grain radius in olivine before transformation is 0.5 μm. In all experiments, the mean radius of wadsleyite grains after full transformation is above 0.5 μm. We can hence conclude that, in experiments LTC_03_02 and LTC_05_01, olivine grain size before transformation is already close to that of the newly formed wadsleyite grains. The phase transformation hence does not result in grain size reduction in these experiments.

Overall, the grain sizes in our experiments are small with an estimated mean grain size equal to or smaller than 1 μm in equivalent radius (except for the starting single crystal of Olivine_01). The differences in mean wadsleyite grain sizes between experiments can be explained by the grain size in the starting material. Neverthe-
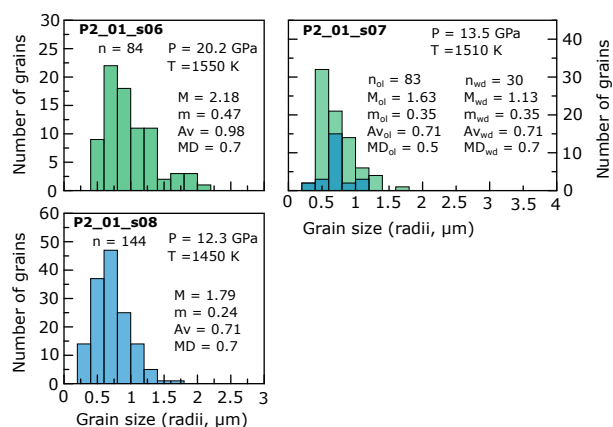
FIGURE 6. Distribution of estimated grain equivalent radii in experiment P2_01 while the sample is pure olivine (collection s06), a mixed olivine-wadsleyite phase (collection s07), and fully transformed to wadsleyite (collection s08). The green and blue bars correspond to olivine and wadsleyite grains size, respectively. n is the number of grains for each phase. M, m, and Av are the maximum, minimum, and average grain radii, respectively. MD is the grain radius for which distribution is maximal. All are expressed in micrometers.

less, wadsleyite grain sizes are somewhat similar in all experiments and we do not see a clear effect of the pressure medium. More investigations will be needed, however, to conclude on the relative effects of stress, overpressure, and pressure media on wadsleyite grain sizes after transformation. In all cases, large olivine crystals tend to disappear during the transformation, with olivine grain radii of about 0.8 μm in equivalent radius in coexisting olivine and wadsleyite. The wadsleyite grains past phase transformation have mean grain radii between 0.5 and 0.8 μm.

DISCUSSION

Olivine-wadsleyite transformation mechanism

We observe lattice preferred orientations in wadsleyite after transformation, with [100] crystallographic axis parallel or at 30–40° of the compression direction in experiments LTC_05_01 and LTC_03_02 (Fig. 5). Starting from an olivine single-crystal (Olivine_01, Fig. 4), wadsleyite after transformation also shows a similar LPO, although weaker than in experiments LTC_05_01 and LTC_03_02.

Experiment P2_01, starting from polycrystalline olivine and for which measurements in the mixed olivine-wadsleyite phase are available, shows a more complex behavior. The first wadsleyite grains nucleate with orientations between the (010) and (001) poles of the IPF of the compression direction (Fig. 5 s07). After the transformation (collection s08), the orientation distribution spreads, with clusters of orientations near the (010), (001), and (100) poles of the IPF, which could be a transition between the first nucleation texture (collection s07) and a texture with the [100] crystallographic axis parallel to compression, as in the three other experiments.

A coherent transformation implies a crystallographic orientation relationship between the parent-phase, olivine, and the daughter-phase, wadsleyite. Smyth et al. (2012) report two topotactic relationships for the olivine-wadsleyite coherent

transformation, based on observations in transmission electron microscopy of post-mortem products of the transformation. Type I orientation relationships lead to (100) olivine ∥ {101} wadsleyite and [001] olivine ∥ [010] wadsleyite. Type II orientation relationships lead to {021} wadsleyite ∥ (100) olivine and [100] wadsleyite ∥ [001] olivine. Both Type I and Type II orientation relationships are tested in Figure 7 for experiments LTC_05_01 and LTC_03_02. The results are clear: the orientations of wadsleyite grains observed in the experiment do not correspond to the predictions of either Type I or Type II orientation relationships.

In P2_01, no clear LPO is observed in the olivine grains before the transformation or in the relict olivine grains coexisting with wadsleyite during transformation. Based on our simulations (Fig. 7), coherent transformations of polycrystalline olivine with no LPO should produce daughter-wadsleyite with no LPO. However, the first wadsleyite grains observed during the transformation show a relatively strong LPO along a girdle between the (010) and (001) poles of the IPF of the compression direction. Hence a coherent transformation cannot explain the transformation texture (nor the post-transformation texture) of the newly formed wadsleyite in this experiment.

Experiments on polycrystalline olivine hence show that orientation relationships observed at the local scale do not apply at the polycrystal scale. As discussed in Smyth et al. (2012), incoherent grains of wadsleyite dominate the sample microstructure. This result is confirmed with experiment Olivine_01, starting from a single crystal, in which multiple domains of wadsleyite and olivine are formed during transformation, with

no obvious orientation relation to the original single-crystal. As such, the inheritance of crystallographic preferred orientations in the olivine-wadsleyite transformation is unlikely to be significant at the 410 km depth discontinuity in the Earth mantle, with a dominant incoherent nucleation of wadsleyite. LPO in wadsleyite during or after transformation is most likely related to oriented growth due to stress or plastic deformation following the phase transformation.

Interestingly, the grain size observed in wadsleyite in our LH-DAC experiments is close to those observed in multi-anvil press experiments at 1400–1800 K with durations ranging from tens of minutes to a few hours (Nishihara et al. 2006; Demouchy et al. 2011; Mohiuddin and Karato 2018). This observation supports that transformation mechanisms in our LH-DAC experiments should not be significantly different than that deduced from large-volume press experiments.

Effect of grain size on the transformation mechanism

The study of Kerschhofer et al. (1996) shows that the grain size of the transforming olivine influences the olivine-wadsleyite transformation mechanism with: (1) a grain-boundary nucleation of wadsleyite, operating in both a large single crystal and a fine grained matrix, and (2) an intracrystalline nucleation of wadsleyite inside a large olivine single crystal only. None of these mechanisms are reported to produce strict orientation relationships between olivine and wadsleyite.

In our polycrystalline experiments, the mean grain size of the parent-olivine is up to 1.0 μm in equivalent radius and hence is smaller than that of the fine matrix of the experiments of
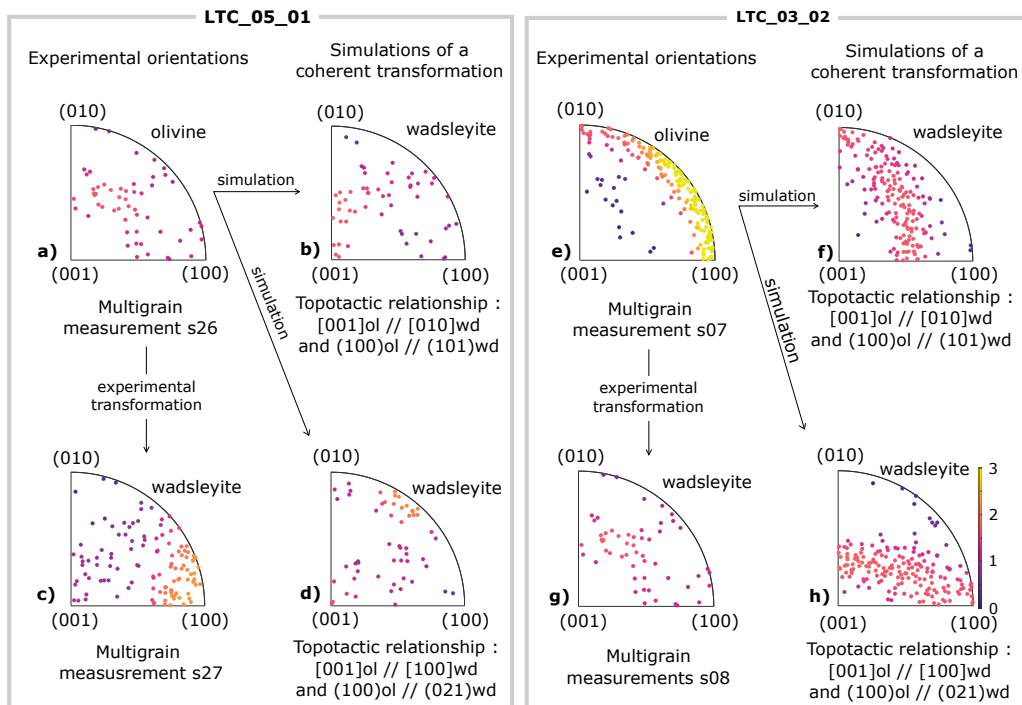
Figure 7. Coherent transformation simulations (**b, d, f,** and **h**) and comparison with the experimental results (**a, c, e,** and **g**), for experiments LTC_05_01 (**a, b, c,** and **d**), and LTC_03_02 (**e, f, g,** and **h**). For each experiment, the olivine grain orientations before transformation (**a** and **e**) are used to compute the daughter wadsleyite orientations. The computation is based on the two topotactic relationships given by Smyth et al. (2012), indicated below the corresponding inverse pole figures. Panels **c** and **g** are experimental wadsleyite grains orientations just after the transformation.

Kerschhofer et al. (1996), where the grain-boundary nucleation is dominant. In experiment Olivine_01 the single-crystal olivine sample is shown to subdivide into multiple domains of both olivine and wadsleyite as the phase transition proceeds (e.g., Fig. 4), leading to an average grain radius of 0.8 µm both in olivine and wadsleyite. According to Kerschhofer et al. (1996), the phase transition, in this case, should also be controlled by a dominant grain-boundary nucleation mechanism.

Mohiuddin and Karato (2018) also found wadsleyite grains of small size (2.8–4.2 µm in diameter) and proposed dominant grain-boundary nucleation of wadsleyite, but at the condition that the transformation over-pressure is below 3 GPa. As over-pressure increases, they showed that intra-crystalline nucleation makes a significant contribution to the volume fraction transformed. In our experiments Olivine_01, LTC_05_01, and LTC_03_02, the transformation over-pressure was less or equal to 3 GPa, and so should be dominated by grain-boundary nucleation of wadsleyite, in agreement with the proposition of Kerschhofer et al. (1996). In experiment P2_01, although grain size is similar to that of the other samples, the over-pressure is larger than 3 GPa. Thus, based on the results of Mohiuddin and Karato (2018), a greater contribution of the intra-crystalline mechanism for wadsleyite nucleation could be expected in this particular experiment.

Effect of stress on the phase transformation

Transformation mechanisms in the olivine system are known to be sensitive to parameters such as stress, temperature, and over-pressure (e.g., Burnley and Green 1989; Burnley et al. 1995; Kerschhofer et al. 1996, 1998; Smyth et al. 2012, and references therein). Early diamond-anvil cell experiments provided inconsistent results, probably due to the lack of pressure-transmitting media and high stresses (Burnley et al. 1995).

Our experiments are performed at much higher temperatures, thanks to laser heating, and use different pressure media, MgO, alumina, and KCl, all with different strengths. They lead to consistent results: the wadsleyite microstructures after transformation from olivine are dominated by an incoherent mechanism, whatever the pressure medium or over-pressure prior to the transformation, with no effect of the olivine starting texture or grain sizes, and consistent grain sizes in wadsleyite past transformation (e.g., Table 2). This is consistent with observations in low-stress and small grain sizes experiments in large-volume press experiments (e.g., Burnley and Green 1989; Kerschhofer et al. 1996; Smyth et al. 2012). A more precise analysis of the effect of stress on the phase transformation mechanism would require a proper estimate of stress in the olivine and wadsleyite grains. Grain-to-grain stress estimate can be obtained using 3D-XRD (e.g., Oddershede et al. 2010; Chandler et al. 2021a) but requires careful calibration for relevant measurements. We did attempt to extract grain-level stress distributions from our data sets but did not obtain reliable results. This will have to be the topic of future investigations.

Over-pressure, stress, and subsequent deformation may have affected details of grain orientations in wadsleyite past transformation from olivine (e.g., Figs. 4 and 5), but the fine analysis of these features goes beyond the goals of this paper.

IMPLICATIONS

Olivine and wadsleyite are considered the main minerals of the upper mantle and the upper section of the MTZ, respectively. Hence, microstructures in these phases have a great influence on the properties of these two layers. It is now largely accepted that LPO induced by olivine deformation is the source of the strong seismic anisotropy measured in the upper mantle (Nishimura and Forsyth 1989; Cara and Lévêque 1988; Long and Becker 2010). Textured downwelling olivine of the upper mantle then transforms into wadsleyite at depths of the 410 km depth discontinuity and questions arise whether this LPO will propagate to wadsleyite in the MTZ.

In agreement with previous ex-situ studies based on electron microscopy (Brearley et al. 1992; Kerschhofer et al. 1996, 1998; Kubo et al. 1998b, 2004; Smyth et al. 2012; Mohiuddin and Karato 2018), our in situ high-pressure high-temperature measurements show that the transformation is dominated by incoherent nucleation at pressures between 12.3 and 20.2 GPa, and temperatures of 1450–1770 K. The result is also confirmed by experiments starting from a larger single-crystal olivine grain.

Thus, our results argue that the olivine to wadsleyite transformation around the 410 km depth will erase the LPO and, also, the whole microstructure of the parent-olivine. As such, the olivine to wadsleyite phase transformation cannot be a source of LPO in the transition zone. Accordingly, seismic anisotropy in olivine will be erased as rocks cross the 410 km depth discontinuity. This is consistent with seismic observations from the literature, which report a significant decrease of the seismic anisotropy in the MTZ compared to the upper mantle (e.g., Fischer and Wien 1996; Panning and Romanowicz 2006; Foley and Long 2011; Yuan and Beghein 2013; Huang et al. 2019). Based on these results, the seismic anisotropy observed in this region (Panning and Romanowicz 2006; Yuan and Beghein 2013; Foley and Long 2011; Huang et al. 2019) should rather arise from additional plastic deformation below the transition zone.

After transformation, the size of the resulting wadsleyite grains in our experiments ranges between 0.4 and 0.8 µm in mean equivalent radius. This result is consistent with other experimental studies on the olivine-wadsleyite transformation, where the newly formed wadsleyite grains are generally on the order of micrometers or tens of micrometers (Smyth et al. 2012; Perrillat et al. 2013; Rosa et al. 2016; Mohiuddin and Karato 2018). Hence, if the grain size of the parent olivine is larger, as it may be expected in the upper mantle (millimeter to centimeter, Faul and Jackson 2005), the transformation would imply a grain size reduction. Grain size is an important parameter in the mechanical properties of rocks as it can change the dominant deformation mechanism of the aggregate. This change of dominant deformation mechanisms (dislocation creep vs. diffusion creep vs. grain boundary sliding) due to grain size variations in the mantle was investigated by numerical studies (e.g., Rozel 2012; Dannberg et al. 2017), which show that grain size variations can modify the rheology and convection of the mantle. In addition, using numerical calculations based on experimental data, Mohiuddin and Karato (2018) show that slab materials at lower temperatures (i.e., small-grain size) will be weaker than slabs at higher temperatures (large-grain size) due to sluggish

grain growth. According to our measurements, the olivine-wadsleyite phase transformation will nucleate small wadsleyite grains, and hence induce a weakening of the aggregate, which will be important to model deformation and the dynamics of the Earth's transition zone.

Finally, the study highlights the potential of using multigrain X-ray diffraction in the laser-heated diamond-anvil cell for the study of microstructures in Earth mantle minerals. Unlike other techniques, such as radial X-ray diffraction, multigrain X-ray diffraction can be combined with laser-heating, approaching both relevant mantle pressure and temperature conditions and maintaining a low level of stress on the sample. In addition, the method allows for extracting statistical information on individual grain sizes and orientations, hence offering new avenues for discoveries in high-pressure mineralogical science.

REFERENCES CITED

Akaogi, M., Ito, E., and Navrotsky, A. (1989) Olivine-modified spinel-spinel transitions in the system Mg_2SiO_4-Fe_2SiO_4: Calorimetric measurements, thermochemical calculation, and geophysical application. Journal of Geophysical Research, 94 (B11), 15671–15685, https://doi.org/10.1029/JB094iB11p15671.

Angel, R.J., Alvaro, M., and Gonzalez-Platas, J. (2014) Eosfit7c and a Fortran module (library) for equation of state calculations. Zeitschrift für Kristallographie: Crystalline Materials, 229, 405–419, https://doi.org/10.1515/zkri-2013-1711.

Angel, R.J., Alvaro, M., and Nestola, F. (2018) 40 years of mineral elasticity: A critical review and a new parameterisation of equations of state for mantle olivines and diamond inclusions. Physics and Chemistry of Minerals, 45, 95–113, https://doi.org/10.1007/s00269-017-0900-7.

Bachmann, F., Hielscher, R., and Schaeben, H. (2010) Texture analysis with MTEX – Free and open source software toolbox. Diffusion and Defect Data, Solid State Data. Part B, Solid State Phenomena, 160, 63–68, https://doi.org/10.4028/www.scientific.net/SSP.160.63.

Bercovici, D. and Karato, S. (2003) Whole-mantle convection and the transition-zone water filter. Nature, 425, 39–44, https://doi.org/10.1038/nature01918.

Brearley, A.J., Rubie, D.C., and Ito, E. (1992) Mechanisms of the transformations between the α, β and γ polymorphs of Mg_2SiO_4 at 15 GPa. Physics and Chemistry of Minerals, 18, 343–358, https://doi.org/10.1007/BF00199415.

Burnley, P.C. and Green, H.W. II (1989) Stress dependence of the mechanism of the olivine–spinel transformation. Nature, 338, 753–756, https://doi.org/10.1038/338753a0.

Burnley, P.C., Bassett, W.A., and Wu, T.C. (1995) Diamond anvil cell study of the transformation mechanism from the olivine to spinel phase in Co_2SiO_4, Ni_2SiO_4, and Mg_2GeO_4. Journal of Geophysical Research, 100 (B9), 17715–17723, https://doi.org/10.1029/95JB01578.

Bykova, E., Aprilis, G., Bykov, M., Glazyrin, K., Wendt, M., Wenz, S., Liermann, H.P., Roeh, J.T., Ehnes, A., Dubrovinskaia, N., and Dubrovinsky, L. (2019) Single-crystal diffractometer coupled with double-sided laser heating system at the Extreme Conditions Beamline P02.2 at PETRA III. Review of Scientific Instruments, 90, 073907, https://doi.org/10.1063/1.5108881.

Cara, M. and Lévêque, J.J. (1988) Anisotropy of the asthenosphere: The higher mode data of the pacific revisited. Geophysical Research Letters, 15, 205–208, https://doi.org/10.1029/GL015i003p00205.

Chandler, B., Bernier, J., Diamond, M., Kunz, M., and Wenk, H.R. (2021a) Exploring microstructures in lower mantle mineral assemblages with synchrotron X-rays. Science Advances, 7, eabd3614, https://doi.org/10.1126/sciadv.abd3614.

Chandler, B., Devoe, M., Kunz, M., and Wenk, H.R. (2021b) Using multigrain crystallography to explore the microstructural evolution of the α-olivine to γ-ringwoodite transformation and ε-Mg_2SiO_4 at high pressure and temperature. Minerals,11, 424, https://doi.org/10.3390/min11040424.

Dannberg, J., Eilon, Z., Faul, U., Gassmöller, R., Moulik, P., and Myhill, R. (2017) The importance of grain size to mantle dynamics and seismological observations. Geochemistry, Geophysics, Geosystems, 18, 3034–3061, https://doi.org/10.1002/2017GC006944.

Demouchy, S., Mainprice, D., Tommasi, A., Couvy, H., Barou, F., Frost, D.J., and Cordier, P. (2011) Forsterite to wadsleyite phase transformation under shear stress and consequences for the Earth's mantle transition zone. Physics of the Earth and Planetary Interiors, 184, 91–104, https://doi.org/10.1016/j.pepi.2010.11.001.

Dziewoński, A.M. and Anderson, D.L. (1981) Preliminary reference Earth model. Physics of the Earth and Planetary Interiors, 25, 297–356, https://doi.org/10.1016/0031-9201(81)90046-7.

Eikenberry, E., Brönnimann, C., Hülsen, G., Toyokawa, H., Horisberger, R., Schmitt, B., Schulze-Briese, C., and Tomizaki, T. (2003) PILATUS: A two-dimensional X-ray detector for macromolecular crystallography. Nuclear Instruments & Methods in Physics Research. Section A, Accelerators, Spectrometers, Detectors and Associated Equipment, 501, 260–266, https://doi.org/10.1016/S0168-9002(02)02044-2.

Faul, U. and Jackson, I. (2005) The seismological signature of temperature and grain size variations in the upper mantle. Earth and Planetary Science Letters, 234, 119–134, https://doi.org/10.1016/j.epsl.2005.02.008.

Fischer, K.M. and Wien, D.A. (1996) The depth distribution of mantle anisotropy beneath the Tonga subduction zone. Earth and Planetary Science Letters, 142(1–2), 253–260, https://doi.org/10.1016/0012-821X(96)00084-2.

Foley, B.J. and Long, M.D. (2011) Upper and mid-mantle anisotropy beneath the Tonga slab: Anisotropy beneath Tonga slab. Geophysical Research Letters, 38, L02303, https://doi.org/10.1029/2010GL046021.

Helffrich, G.R. and Wood, B.J. (1996) 410 km discontinuity sharpness and the form of the olivine α–β phase diagram: Resolution of apparent seismic contradictions. Geophysical Journal International, 126, F7–F12, https://doi.org/10.1111/j.1365-246X.1996.tb05292.x.

Huang, Q., Schmerr, N., Waszek, L., and Beghein, C. (2019) Constraints on seismic anisotropy in the mantle transition zone from long-period SS precursors. Journal of Geophysical Research. Solid Earth, 124, 6779–6800, https://doi.org/10.1029/2019JB017307.

Ito, E. and Katsura, T. (1989) A temperature profile of the mantle transition zone. Geophysical Research Letters, 16, 425–428, https://doi.org/10.1029/GL016i005p00425.

Katsura, T. and Ito, E. (1989) The system Mg_2SiO_4-Fe_2SiO_4 at high pressures and temperatures: Precise determination of stabilities of olivine, modified spinel, and spinel. Journal of Geophysical Research, 94(B11), 15663–15670, https://doi.org/10.1029/JB094iB11p15663.

Katsura, T., Yamada, H., Nishikawa, O., Song, M., Kubo, A., Shinmei, T., Yokoshi, S., Aizawa, Y., Yoshino, T., Walter, M.J., and others. (2004) Olivine-wadsleyite transition in the system $(Mg,Fe)_2SiO_4$. Journal of Geophysical Research: Solid Earth, 109, B02209, https://doi.org/10.1029/2003JB002438.

Katsura, T., Shatskiy, A., Manthilake, M.A.G.M., Zhai, S., Yamazaki, D., Matsuzaki, T., Yoshino, T., Yoneda, A., Ito, E., Sugita, M., and others. (2009) P-V-T relations of wadsleyite determined by in situ X-ray diffraction in a large-volume high-pressure apparatus. Geophysical Research Letters, 36, L11307, https://doi.org/10.1029/2009GL038107.

Kavner, A. and Duffy, T.S. (2001) Pressure-volume-temperature paths in the laser-heated diamond anvil cell. Journal of Applied Physics, 89, 1907–1914, https://doi.org/10.1063/1.1335827.

Kerschhofer, L., Sharp, T.G., and Rubie, D.C. (1996) Intracrystalline transformation of olivine to wadsleyite and ringwoodite under subduction zone. Science, 274, 79–81, https://doi.org/10.1126/science.274.5284.79.

Kerschhofer, L., Dupas, C., Liu, M., Sharp, T.G., Durham, W.B., and Rubie, D.C. (1998) Polymorphic transformations between olivine, wadsleyite and ringwoodite: Mechanisms of intracrystalline nucleation and the role of elastic strain. Mineralogical Magazine, 62, 617–638, https://doi.org/10.1180/002646198548016.

Kimura, T., Ohfuji, H., Nishi, M., and Irifune, T. (2017) Melting temperatures of MgO under high pressure by micro-texture analysis. Nature Communications, 8, 15735, https://doi.org/10.1038/ncomms15735.

Kubo, T., Ohtani, E., Kato, T., Shinmei, T., and Fujino, K. (1998a) Effects of water on the alpha-beta transformation kinetics in San Carlos olivine. Science, 281,

85–87, https://doi.org/10.1126/science.281.5373.85.

——— (1998b) Experimental investigation of the α-β transformation of San Carlos olivine single crystal. Physics and Chemistry of Minerals, 26, 1–6, https://doi.org/10.1007/s002690050155.

Kubo, T., Ohtani, E., and Funakoshi, K.I. (2004) Nucleation and growth kinetics of the α–β transformation in Mg$_2$SiO$_4$ determined by in-situ synchrotron powder X-ray diffraction. American Mineralogist, 89, 285–293, https://doi.org/10.2138/am-2004-2-305.

Langrand, C., Hilairet, N., Nisr, C., Roskosz, M., Ribárik, G., Vaughan, G.B.M., and Merkel, S. (2017) Reliability of multigrain indexing for orthorhombic polycrystals above 1 Mbar: Application to MgSiO$_3$ post-perovskite. Journal of Applied Crystallography, 50, 120–130, https://doi.org/10.1107/S1600576716018057.

Ledoux, E., Krug, M., Gay, J., Chantel, J., Hilairet, N., Bykov, M., Bykova, E., Aprilis, G., Svitlyk, V., Garbarino, G., and others. (2023) Data supporting the article "In-situ study of microstructures induced by the olivine to wadsleyite transformation at conditions of the 410 km depth discontinuity" by Ledoux et al.", https://doi.org/10.57745/NZFWP9, Recherche Data Gouv.

Liermann, H.P., Konôpková, Z., Morgenroth, W., Glazyrin, K., Bednarčik, J., McBride, E.E., Petitgirard, S., Delitz, J.T., Wendt, M., Bican, Y., and others. (2015) The extreme conditions beamline P02.2 and the extreme conditions science infrastructure at PETRA III. Journal of Synchrotron Radiation, 22, 908–924, https://doi.org/10.1107/S1600577515005937.

Long, M.D. and Becker, T.W. (2010) Mantle dynamics and seismic anisotropy. Earth and Planetary Science Letters, 297, 341–354, https://doi.org/10.1016/j.epsl.2010.06.036.

Lutterotti, L., Vasin, R., and Wenk, H.R. (2014) Rietveld texture analysis from synchrotron diffraction images. I. Calibration and basic analysis. Powder Diffraction, 29, 76–84, https://doi.org/10.1017/S0885715613001346.

Mohiuddin, A. and Karato, S.I. (2018) An experimental study of grain-scale microstructure evolution during the olivine-wadsleyite phase transition under nominally 'dry' conditions. Earth and Planetary Science Letters, 501, 128–137, https://doi.org/10.1016/j.epsl.2018.08.039.

Mohiuddin, A., Karato, S.I., and Girard, J. (2020) Slab weakening during the olivine to ringwoodite transition in the mantle. Nature Geoscience, 13, 170–174, https://doi.org/10.1038/s41561-019-0523-3.

Nishihara, Y., Shinmei, T., and Karato, S.I. (2006) Grain-growth kinetics in wadsleyite: Effects of chemical environment. Physics of the Earth and Planetary Interiors, 154, 30–43, https://doi.org/10.1016/j.pepi.2005.08.002.

Nishimura, C.E. and Forsyth, D.W. (1989) The anisotropic structure of the upper mantle in the pacific. Geophysical Journal International, 96, 203–229, https://doi.org/10.1111/j.1365-246X.1989.tb04446.x.

Nisr, C., Ribárik, G., Ungár, T., Vaughan, G.B.M., Cordier, P., and Merkel, S. (2012) High resolution three-dimensional X-ray diffraction study of dislocations in grains of MgGeO$_3$ post-perovskite at 90 GPa. Journal of Geophysical Research: Solid Earth, 117, https://doi.org/10.1029/2011JB008401.

Nisr, C., Ribárik, G., Ungár, T., Vaughan, G.B., and Merkel, S. (2014) Three-dimensional X-ray diffraction in the diamond anvil cell: Application to stishovite. High Pressure Research, 34, 158–166, https://doi.org/10.1080/08957959.2014.885021.

Oddershede, J., Schmidt, S., Poulsen, H.F., Sørensen, H.O., Wright, J., and Reimers, W. (2010) Determining grain resolved stresses in polycrystalline materials using three-dimensional X-ray diffraction. Journal of Applied Crystallography, 43, 539–549, https://doi.org/10.1107/S0021889810012963.

Panning, M. and Romanowicz, B. (2006) A three-dimensional radially anisotropic model of shear velocity in the whole mantle. Geophysical Journal International, 167, 361–379, https://doi.org/10.1111/j.1365-246X.2006.03100.x.

Perrillat, J.P., Daniel, I., Bolfan-Casanova, N., Chollet, M., Morard, G., and Mezouar, M. (2013) Mechanism and kinetics of the α–β transition in San Carlos olivine Mg$_{1.8}$Fe$_{0.2}$SiO$_4$. Journal of Geophysical Research. Solid Earth, 118, 110–119, https://doi.org/10.1002/jgrb.50061.

Poirier, J.P. and Guillopé, M. (1979) Deformation induced recrystallization of minerals. Bulletin de Minéralogie (Paris), 102, 67–74, https://doi.org/10.3406/bulmi.1979.7256.

Prescher, C. and Prakapenka, V.B. (2015) DIOPTAS: A program for reduction of two-dimensional X-ray diffraction data and data exploration. High Pressure Research, 35, 223–230, https://doi.org/10.1080/08957959.2015.1059835.

Ringwood, A.E. (1958) The constitution of the mantle—II: Further data on the olivine-spinel transition. Geochimica et Cosmochimica Acta, 15, 18–29, https://doi.org/10.1016/0016-7037(58)90005-X.

——— (1962) Prediction and confirmation of olivine-spinel transition in Ni$_2$SiO$_4$. Geochimica et Cosmochimica Acta, 26, 457–469, https://doi.org/10.1016/0016-7037(62)90090-X.

——— (1991) Phase transformations and their bearing on the constitution and dynamics of the mantle. Geochimica et Cosmochimica Acta, 55, 2083–2110,

https://doi.org/10.1016/0016-7037(91)90090-R.

Ringwood, A.E. and Seabrook, M. (1962) Olivine-spinel equilibria at high pressure in the system Ni$_2$GeO$_4$-Mg$_2$SiO$_4$. Journal of Geophysical Research, 67, 1975–1985, https://doi.org/10.1029/JZ067i005p01975.

Rosa, A.D., Hilairet, N., Ghosh, S., Garbarino, G., Jacobs, J., Perrillat, J.P., Vaughan, G., and Merkel, S. (2015) In situ monitoring of phase transformation microstructures at Earth's mantle pressure and temperature using multigrain XRD. Journal of Applied Crystallography, 48, 1346–1354, https://doi.org/10.1107/S1600576715012765.

Rosa, A.D., Hilairet, N., Ghosh, S., Perrillat, J.P., Garbarino, G., and Merkel, S. (2016) Evolution of grain sizes and orientations during phase transitions in hydrous Mg$_2$SiO$_4$. Journal of Geophysical Research. Solid Earth, 121, 7161–7176, https://doi.org/10.1002/2016JB013360.

Ross, N.L. and Navrotsky, A. (1987) The Mg$_2$GeO$_4$ olivine-spinel phase transition. Physics and Chemistry of Minerals, 14, 473–481, https://doi.org/10.1007/BF00628825.

Rozel, A. (2012) Impact of grain size on the convection of terrestrial planets. Geochemistry, Geophysics. Geosystems, 13, Q10020, https://doi.org/10.1029/2012GC004282.

Saki, M., Thomas, C., Merkel, S., and Wookey, J. (2018) Detecting seismic anisotropy above the 410 km discontinuity using reflection coefficients of underside reflections. Physics of the Earth and Planetary Interiors, 274, 170–183, https://doi.org/10.1016/j.pepi.2017.12.001.

Schmidt, S. (2014) GrainSpotter: A fast and robust polycrystalline indexing algorithm. Journal of Applied Crystallography, 47, 276–284, https://doi.org/10.1107/S1600576713030185.

Shen, G. and Lazor, P. (1995) Measurement of melting temperatures of some minerals under lower mantle pressures. Journal of Geophysical Research, 100(B9), 17699–17713, https://doi.org/10.1029/95JB01864.

Smyth, J.R., Miyajima, N., Huss, G.R., Hellebrand, E., Rubie, D.C., and Frost, D.J. (2012) Olivine-wadsleyite-pyroxene topotaxy: Evidence for coherent nucleation and diffusion-controlled growth at the 410-km discontinuity. Physics of the Earth and Planetary Interiors, 200-201, 85–91, https://doi.org/10.1016/j.pepi.2012.04.003.

Sörensen, H.O., Schmidt, S., Wright, J.P., Vaughan, G.B.M., Techert, S., Garman, E.F., Oddershede, J., Davaasambuu, J., Paithankar, K.S., Gundlach, C., and others. (2012) Multigrain crystallography. Zeitschrift für Kristallographie, 227, 63–78, https://doi.org/10.1524/zkri.2012.1438.

Urai, J.L., Means, W.D., and Lister, G.S. (1986) Dynamic recrystallization of minerals. Mineral and Rock Deformation: Laboratory Studies, 36, 161–199, https://doi.org/10.1029/GM036p0161.

Vaughan, P.J. and Coe, R.S. (1981) Creep mechanism in Mg$_2$GeO$_4$: Effects of a phase transition. Journal of Geophysical Research, 86(B1), 389, https://doi.org/10.1029/JB086iB01p00389.

Wenk, H.R., Lonardeli, I., Pehl, J., Devine, J., Prakapenka, V., Shen, G., and Mao, H.K. (2004) In situ observation of texture development in olivine, ringwoodite, magnesiowüstite and silicate perovskite at high pressure. Earth and Planetary Science Letters, 226, 507–519, https://doi.org/10.1016/j.epsl.2004.07.033.

Wenk, H.R., Lutterotti, L., Kaercher, P., Kanitpanyacharoen, W., Miyagi, L., and Vasin, R. (2014) Rietveld texture analysis from synchrotron diffraction images. II. Complex multiphase materials and diamond anvil cell experiments. Powder Diffraction, 29, 220–232, https://doi.org/10.1017/S0885715614000360.

Wright, J.P. (2006) ImageD11. ImageD11 is a Python code for identifying individual grains in spotty area detector X-ray diffraction data. ESRF, Grenoble, France, https://github.com/FABLE-3DXRD/ImageD11.

Yuan, K. and Beghein, C. (2013) Seismic anisotropy changes across upper mantle phase transitions. Earth and Planetary Science Letters, 374, 132–144, https://doi.org/10.1016/j.epsl.2013.05.031.

Zhang, L., Yuan, H., Meng, Y., and Mao, H.K. (2019) Development of high-pressure multigrain X-ray diffraction for exploring the Earth's interior. Engineering, 5, 441–447, https://doi.org/10.1016/j.eng.2019.02.004.

Zhou, D., Dong, J., Si, Y., Zhu, F., and Li, J. (2020) Melting curve of potassium chloride from in situ ionic conduction measurements. Minerals, 10, 250, https://doi.org/10.3390/min10030250.